Title

Diffractive Imaging of Transient Electronic Coherences in Molecules with Electron Vortices

Journal

Physical Review Letters, 134(7)

ISSN

0031-9007

Authors

Wu, Haowei

Yong, Haiwang

Publication Date

2025-02-21

DOI

10.1103/physrevlett.134.073001

Peer reviewed

Diffractive imaging of transient electronic coherences in molecules with electron vortices

Authors: Haowei Wu[1], Haiwang Yong[1,2]*

Affiliations:

[1]Department of Chemistry and Biochemistry, University of California San Diego, La Jolla, CA 92093

[2]Program in Materials Science and Engineering, University of California San Diego, La Jolla, CA 92093

*Correspondence to: hyong@ucsd.edu (H. Y.)

Abstract

Direct imaging of transient electronic coherences in molecules has been challenging, with the potential to control electron motions and influence reaction outcomes. We propose a novel time-resolved vortex electron diffraction technique to spatially resolve transient electronic coherences in isolated molecules. By analyzing helical dichroism diffraction signals, the contribution of electronic populations cancels out, isolating the purely electronic coherence signals. This allows direct monitoring of the time evolution and decoherence of transient electronic coherences in molecules.

Main Text

The exact total molecular wavefunction can be factorized as a product of electronic and nuclear wavefunctions [1,2]. The Born-Oppenheimer approximation further treats nuclear motion as proceeding in a potential energy surface of an adiabatic electronic state, forming the foundation of modern quantum chemistry and molecular physics. The development of coherent femtosecond laser pulses in 1980s [3], with bandwidths of tens of millielectronvolts (meV), enables the creation of superpositions of multiple vibrational states (i.e. vibrational coherences) in molecules, resulting in coherent nuclear motions. This gave birth to "femtochemistry" [4], which focuses on tracking the nuclear motion in molecules that

governs the chemical reaction. Over the last 20 years, the rapid development of attosecond pulses [5,6] has pushed the field into the era of "attochemistry". The much broader bandwidth (a few eV) of coherent attosecond pulse allows for the generation of superpositions of multiple electronic states (electronic coherences) in molecules, exhibiting coherent electronic motions. Electronic coherence manifests not only as attosecond electron dynamics in molecules immediately after laser excitation, but also arises during nonradiative electronic relaxations facilitated by conical intersections. At conical intersections, two or more electronic states become degenerate, resulting in a breakdown of Born-Oppenheimer approximation. The role of electronic coherences in molecules has therefore become the key to understanding various photochemical and photophysical processes, with the potential to control electron motions in molecules and influence reaction outcomes [7–9].

Measurements of transient electronic coherences in molecules have garnered increasing interest [10–15]. However, there are two major challenges remaining in the field. The first is probing exclusively electronic coherence contributions to the signal with no contribution from electronic populations. The second is achieving real-space imaging of the associated time-dependent evolution of electron density. To address these challenges, several novel experimental concepts have been proposed. One notable example is the Transient Redistribution of Ultrafast Electronic Coherences in Attosecond Raman Signals (TRUECARS) [16]. This proposed technique holds the promise to detect energy profiles of electronic coherences without contributions from populations. Furthermore, a twisted X-ray diffraction technique has been proposed with the potential to exclusively image the spatial profiles of transient charge densities associated with electronic coherence [17]. However, its experimental realization still requires enormous efforts due to its reliance on large-scale facilities, such as X-ray Free-electron Lasers, which can generate hard X-rays with attosecond pulse durations and extreme brightness.

This could become feasible in the future with the ongoing development of such light sources worldwide, though it still faces the challenge of limited accessibility, as only a few such large facilities are currently available [18]. Exploring whether this concept could be adapted to ultrafast electron diffraction (UED) presents an intriguing alternative, offering several advantages over X-ray diffraction: a scattering cross-section ~6 orders of magnitude larger, access to larger momentum transfer ranges due to the very short de Broglie wavelength of electrons, and a substantially smaller, more accessible setup that can fit within small research facilities [19–21].

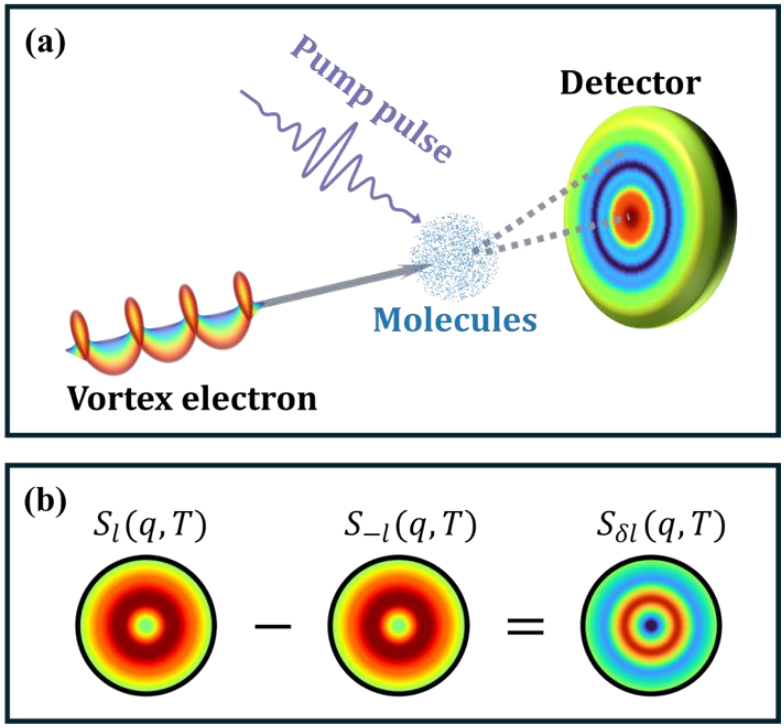

Figure 1. Schematic description of (a) Vortex-UED experiments and (b) the helical dichroism diffraction signal of Vortex-UED.

In this Letter, we theoretically propose a novel time-resolved electron diffraction technique capable of spatially resolving transient electronic coherences in isolated molecules exclusively, without contributions from electronic populations. The method, Vortex Ultrafast Electron Diffraction (Vortex-UED), probes transient electronic coherences in isolated molecules via ultrafast electron diffraction

using electron vortices rather than plane waves (see Figure 1a). Electron vortices are free electrons carrying orbital angular momentum (OAM, denoted as l), characterized by a spiraling wavefront with a screw dislocation along the propagation axis [22–25]. The l represents the magnitude of the OAM (also known as topological charge), which can be any integer value. Various strategies for generating high-quality vortex electron beams have made their application in electron diffraction feasible [26–29]. Recent experiments in time-resolved gas-phase diffraction have enabled direct observation of ultrafast structural changes during chemical reactions [30–34], holding the promise of real-space tracking of both electron and nuclear motions in molecules. Although theoretical studies suggest that standard diffraction signals contain contributions from electronic coherence [35–39], these contributions are typically too small compared to the dominant signals from electronic populations. Therefore, a method to isolate these electronic coherence signals in UED is necessary.

Here, we show that this can be achieved using Vortex-UED. By measuring the rotationally-averaged UED signals using electron vortices with opposite OAMs, we find that the electronic population signals cancel out, leaving only the electronic coherence signals in the helical dichroism diffraction signal of Vortex-UED (see Figure 1b). The helical dichroism diffraction signal here is expressed as

$$S_{\delta l}(q,T) = \langle S_l(\mathbf{q},T)\rangle_\Omega - \langle S_{-l}(\mathbf{q},T)\rangle_\Omega \quad (1)$$

where $S_l(\mathbf{q},T)$ is the Vortex-UED pattern recorded with a vortex electron beam carrying an OAM of l, q is the magnitude of momentum transfer vector $\mathbf{q}$, T is the time delay between the actinic pulse and the electron probe pulse, and $\langle\cdots\rangle_\Omega$ denotes the rotationally-averaged diffraction signal. In the following, we demonstrated through both theoretical derivations and numerical simulations that this helical dichroism diffraction signal, $S_{\delta l}(q,T)$, is sensitive solely to the transient electronic coherences

in molecules. We further illustrate the concept of the proposed technique by applying it to the detection of early attosecond electron dynamics arising from purely electronic coherence and its dephasing in oxazole upon photoexcitation.

The time-dependent molecular many-electron wave function upon photoexcitation can be expressed as

$$|\Psi(t)\rangle = \sum_k c_k(t)|\varphi_k\rangle \tag{2}$$

where $|\varphi_k\rangle$ is the k_{th} adiabatic electronic state, and $c_k(t) = c_{k0}e^{-\frac{i\varepsilon_k t}{\hbar}}$ is the time-dependent amplitude of the electronic state. Here, ε_k represents the energy of the electronic state, $\hbar$ is the reduced Planck constant, and t is the time. Equation 2 assumes purely electronic dynamics with frozen nuclei, which is justified for the early time scales shorter than the typical nuclear vibrational period of molecules (a few femtoseconds).

The real-space time-evolving electronic charge density is given by

$$\begin{aligned}\sigma^{\text{E}}_{\text{tot}}(\mathbf{r},t) = \left\langle \hat{\sigma}^{\text{E}}(\mathbf{r},t)\right\rangle &= \sum_k \rho_{kk}\sigma^{\text{E}}_{kk}(\mathbf{r}) + 2\Re\left[\sum_{j>k}\rho_{jk}(t)\sigma^{\text{E}}_{kj}(\mathbf{r})\right] \\ &= \sigma^{\text{E}}_{\text{pop}}(\mathbf{r}) + \sigma^{\text{E}}_{\text{coh}}(\mathbf{r},t)\end{aligned} \tag{3}$$

where $\mathbf{r}$ is the spatial coordinate, $\sigma^{\text{E}}_{kk}(\mathbf{r})$ is the electronic charge density of the k_{th} electronic state, and $\sigma^{\text{E}}_{kj}(\mathbf{r})$ is the electronic transition charge density between electronic state k and j. The term $\rho_{kk} = c_k^*(t)c_k(t)$ describes the electronic population, which remains constant if there are no transitions between different electronic states. Meanwhile, $\rho_{jk}(t) = c_k^*(t)c_j(t)$ represents the electronic coherence term, which oscillates with a period of $T_{\text{p}} = \frac{2\pi}{\omega_{jk}}$, where $\omega_{jk} = (\varepsilon_j - \varepsilon_k)/\hbar$. The total electronic charge density $\sigma^{\text{E}}_{\text{tot}}(\mathbf{r},t)$ consists of contributions from both the electronic population density $\sigma^{\text{E}}_{\text{pop}}(\mathbf{r})$ and the electronic coherence density $\sigma^{\text{E}}_{\text{coh}}(\mathbf{r},t)$. Note that here the time dependence

of the total charge density arises solely from the coherence density, which is responsible for the time-evolving electron dynamics in molecules.

The theoretical description of the Vortex-UED signal is based on off-resonant time-resolved single-molecule electron diffraction within minimal coupling picture [35,40]. We note that the term 'single-molecule diffraction' here refers to the case of a completely disordered sample, such as gas-phase molecules, to differentiate it from the term "two-molecule diffraction", which applies to a sample possessing long-range order, such as crystals [41]. The single-molecule diffraction signal thus scales as N, while the two-molecule diffraction signal scales as N^2, where N is the number of molecules in the interaction region. A detailed derivation of Vortex-UED signal is provided in the Supplemental Material [42], Note 1. The diffraction signal measures the expectation values of the products of charge-density operators in momentum space, $\langle \hat{\sigma}^{\dagger} \hat{\sigma} \rangle$, allowing direct monitoring of the time-evolving charge density described in Equation 3.

Unlike twisted X-ray diffraction, which is constructed solely from the electronic charge-density operator [17], the Vortex-UED signal is derived from the total charge-density operator, encompassing both electronic and nuclear charge densities as illustrated in Supplemental Material [42], Figure S2. The Vortex-UED signal $S_l(\mathbf{q}, T)$ can thus be partitioned into three components,

$$S_l(\mathbf{q}, T) = S_{\mathrm{E},l}(\mathbf{q}, T) + S_{\mathrm{mix},l}(\mathbf{q}, T) + S_{\mathrm{N},l}(\mathbf{q}, T) \tag{4}$$

where $S_{\mathrm{E},l}(\mathbf{q}, T)$ corresponds to the purely electronic charge density $\sigma^{\mathrm{E}}\sigma^{\mathrm{E}}$, $S_{\mathrm{N},l}(\mathbf{q}, T)$ arises from the purely nuclear charge density $\sigma^{\mathrm{N}}\sigma^{\mathrm{N}}$, and $S_{\mathrm{mix},l}(\mathbf{q}, T)$ contains the mixed nuclear-electronic term $\sigma^{\mathrm{E}}\sigma^{\mathrm{N}}$. Understanding how the additional purely nuclear term $S_{\mathrm{N},l}(\mathbf{q}, T)$ and the mixed nuclear-electronic term $S_{\mathrm{mix},l}(\mathbf{q}, T)$ affect the helical dichroism electron diffraction signal in Equation 1 is essential for assessing its potential to isolate purely electronic coherence signals. Similar to Equation 3,

$S_l(\mathbf{q},T)$ can be further decomposed into contributions from electronic populations $S_l^{\mathrm{pop}}(\mathbf{q},T)$ and coherences $S_l^{\mathrm{coh}}(\mathbf{q},T)$, as follows

$$S_l^{\mathrm{pop}}(\mathbf{q},T) = S_{\mathrm{E},l}^{\mathrm{pop}}(\mathbf{q},T) + S_{\mathrm{mix},l}^{\mathrm{pop}}(\mathbf{q},T) + S_{\mathrm{N},l}^{\mathrm{pop}}(\mathbf{q},T) \tag{5}$$

$$S_l^{\mathrm{coh}}(\mathbf{q},T) = S_{\mathrm{E},l}^{\mathrm{coh}}(\mathbf{q},T) + S_{\mathrm{mix},l}^{\mathrm{coh}}(\mathbf{q},T) \tag{6}$$

Here, $S_{\mathrm{E},l}^{\mathrm{pop/coh}}(\mathbf{q},T)$ and $S_{\mathrm{mix},l}^{\mathrm{pop/coh}}(\mathbf{q},T)$ represent the population/coherence contributions to the electronic and mixed signal, respectively. Note that the purely nuclear term $S_{\mathrm{N},l}(\mathbf{q},T)$ does not contain electronic coherence signatures, as it is constructed solely from the nuclear charge-density operator [35].

We now focus on the helical dichroism diffraction signal defined in Equation 1, $S_{\delta l}(q,T) = \langle S_l(\mathbf{q},T)\rangle_\Omega - \langle S_{-l}(\mathbf{q},T)\rangle_\Omega = S_{\delta l}^{\mathrm{pop}}(q,T) + S_{\delta l}^{\mathrm{coh}}(q,T)$. From the derivations in Supplemental Material [42], Note 2, one can see that the population term vanishes, meaning $S_{\delta l}^{\mathrm{pop}}(q,T) = \left\langle S_l^{\mathrm{pop}}(\mathbf{q},T)\right\rangle_\Omega - \left\langle S_{-l}^{\mathrm{pop}}(\mathbf{q},T)\right\rangle_\Omega = 0$. Furthermore, the mixed coherence term also vanishes in $S_{\delta l}^{\mathrm{coh}}(q,T)$, such that $S_{\mathrm{mix},\delta l}^{\mathrm{coh}}(q,T) = \left\langle \tilde{S}_{\mathrm{mix},l}^{\mathrm{coh}}(\mathbf{q},T)\right\rangle_\Omega - \left\langle \tilde{S}_{\mathrm{mix},-l}^{\mathrm{coh}}(\mathbf{q},T)\right\rangle_\Omega = 0$. Thus, the helical dichroism diffraction signal in Equation 1 reduces to

$$S_{\delta l}(q,T) = S_{\delta l}^{\mathrm{coh}}(q,T) = S_{\mathrm{E},\delta l}^{\mathrm{coh}}(q,T) \tag{7}$$

Equation 7 shows that the helical dichroism diffraction signal is exclusively sensitive to the electronic coherences in the molecule. This is directly related to the electronic coherence density, $\sigma_{\mathrm{coh}}^{\mathrm{E}}(\mathbf{r},t)$, described in Equation 3, with no contributions from the population term associated to $\sigma_{\mathrm{pop}}^{\mathrm{E}}(\mathbf{r})$.

We demonstrate the concept of the proposed technique by applying it to the early attosecond electron dynamics of oxazole following excitation to the ππ* electronic state. Oxazole serves as a critical building block in various pharmaceutical and synthetic intermediates [47,48]. The photoinduced ring-opening dynamics of oxazole and its derivatives have been extensively studied [49,50]. Combined excite-state dynamical simulations and time-resolved photoelectron spectra have indicated that, in

addition to vibrational relaxation in the excite state, a ring-opening dynamics occurs on the order of 100 fs after excitation to the ππ* state [50].

In this study, we assume a 10% excitation fraction of the electronic excited state upon excitation, resulting in a coherent superposition of the ground state, φ_0, and the excited state, φ_1. The evolution of the time-dependent electronic population term ρ_{11} and the electronic coherence term ρ_{10} are shown in Supplemental Material [42], Figure S1. It is evident that the electronic population remains constant over time, while the electronic coherence term oscillates with a period of T_p. We further illustrate the change in electronic population density $\Delta\sigma^{\mathrm{E}}_{\mathrm{pop}}(\mathbf{r})$, which remains static throughout the entire period. The time-dependent electron density changes driven purely by electronic coherence are represented by the difference electronic coherence density $\Delta\sigma^{\mathrm{E}}_{\mathrm{coh}}(\mathbf{r},t)$. A complete period of electron motion in oxazole right after excitation is shown in Supplemental Material [42], Figure S1, with electrons primarily oscillating between the oxygen/nitrogen atoms and the two carbon atoms adjacent to the nitrogen atom. It is important to note that this electron dynamics occurs when there is an overlap between the excited-state nuclear wavepacket and the unexcited ground-state nuclear wavepacket in the very early stages of photoexcitation. This overlap diminishes as the later on nuclear motions proceed over tens of femtoseconds, leading to electronic decoherence. We will explore the effects of the decoherence in our subsequent discussion of the simulated helical dichroism diffraction signal.

In a previous ultrafast X-ray scattering experiment, changes in the electron density distribution upon excitation in molecules have been experimentally observed [51]. However, due to the lack of attosecond temporal resolution and the dominant signal from electronic populations, only the $\Delta\sigma^{\mathrm{E}}_{\mathrm{pop}}(\mathbf{r})$ was detected, while the time-dependent electronic coherence density $\Delta\sigma^{\mathrm{E}}_{\mathrm{coh}}(\mathbf{r},t)$ remained unobserved.

Here, we demonstrate that such attosecond electron dynamics arising from electronic coherences could be observed exclusively in diffraction experiments using Vortex-UED.

The electron dynamics of oxazole is well captured by the helical dichroism diffraction signal shown in Figure 2a. We simulated the time-resolved Vortex-UED signal $S_l(q,T)$ for both $l=1$ and $l=-1$ vortex electron beams. Figure 2a is obtained by taking the difference between these two diffraction signals, as described by Equation 1. In addition to the Vortex-UED signal $S_{\delta l}(q,T)$ for $l=\pm1$, the signals for $l=\pm2$ and $l=\pm3$ are also shown in Supplemental Material [42], Figure S3. All three cases exhibit the same time dependence from the time-evolving electronic coherence term ρ_{10}, but their variation with q reveals different features for vortex beams with distinct topological charges. Since this variation reflects the real-space distribution of electronic coherence density $\Delta\sigma^{\mathrm{E}}_{\mathrm{coh}}(\mathbf{r},t)$, the different topological charges of the OAM beam modulate the charge-density operator as $\hat{\sigma}^{\mathrm{E}}_{l}(\mathbf{q},t)=\int d\mathbf{r}\hat{\sigma}^{\mathrm{E}}(\mathbf{r},t)e^{il\phi}e^{i\mathbf{q}\cdot\mathbf{r}}$. This allows for selective detection of electronic coherence density arising from various electronic transitions with different OAM beams. The numerical simulation results are consistent with our final expression for $S_{\delta l}(q,T)$, which is derived in Supplemental Material [42], Note 2. To further demonstrate that the signal in Figure 2a originates solely from the electronic coherence term, Figure 2b and 2c present the individual terms from Equation 5 and 6 at a specific time point. It is evident that, while the population signal $S^{\mathrm{pop}}_{l}(q,T)$ is much stronger than the coherence signal $S^{\mathrm{coh}}_{l}(q,T)$, all population signals are fully cancelled out when subtracting the l and $-l$ Vortex-UED signals. This leaves only the electronic coherence contribution, as shown in Figure 2d. Additionally, the simulated results align with Equation 7, confirming that only the $S^{\mathrm{coh}}_{\mathrm{E},\delta l}(q,T)$ term contributes to the final signal.

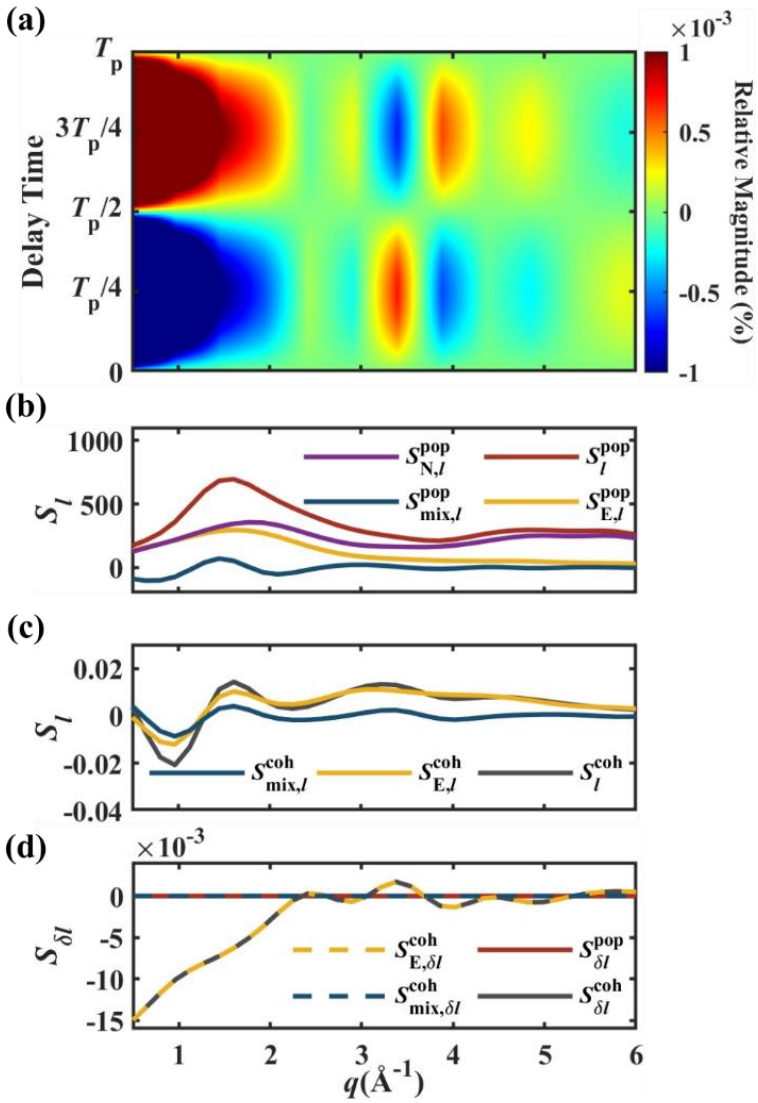

Figure 2. (a) The helical dichroism diffraction signals in Equation 1 over a complete period ($l = \pm 1$). The signals are shown as percentages, $\%S_{\delta l}(q,T) = 100\,\frac{S_{\delta l}(q,T)}{S_l^{\mathrm{off}}(q)}$, where $S_l^{\mathrm{off}}(q)$ is the reference Vortex-UED signal before time zero. (b) Total population contribution $S_l^{\mathrm{pop}}(q,T)$ to the Vortex-UED signal and its decomposition into electronic $S_{\mathrm{E},l}^{\mathrm{pop}}(q,T)$, nuclear $S_{\mathrm{N},l}^{\mathrm{pop}}(q,T)$ and mixed nuclear-electronic $S_{\mathrm{mix},l}^{\mathrm{pop}}(q,T)$ terms ($l = 1$ and $T = T_{\mathrm{p}}/4$). (c) Total coherence contribution $S_l^{\mathrm{coh}}(q,T)$ to the Vortex-UED signal and its decomposition into electronic $S_{\mathrm{E},l}^{\mathrm{coh}}(q,T)$ and mixed nuclear-electronic $S_{\mathrm{mix},l}^{\mathrm{coh}}(q,T)$ terms ($l = 1$ and $T = T_{\mathrm{p}}/4$). (d) Population $S_{\delta l}^{\mathrm{pop}}(q,T)$ and coherence $S_{\delta l}^{\mathrm{coh}}(q,T)$ contributions to the helical dichroism diffraction signals at $T_{\mathrm{p}}/4$. The electronic $S_{\mathrm{E},\delta l}^{\mathrm{coh}}(q,T)$ and mixed nuclear-electronic $S_{\mathrm{mix},\delta l}^{\mathrm{coh}}(q,T)$ terms are also shown.

We further investigate the effect of electronic decoherence on the helical dichroism diffraction signal. The pure electron dynamics of oxazole are expected to decay due to interactions between the electronic system and a nuclear bath. Although these electronic decoherence effects are not included in our electron dynamics simulation, they can be described phenomenologically. Pure dephasing can be accounted for by multiplying the signal expression by a dephasing factor $e^{-\Gamma t}$, where Γ represents the electronic decoherence rate [52]. The full signal expression is provided in Supplemental Material [42], Note 2. Figure 3 compares the time-resolved helical dichroism diffraction signals for two different dephasing rates, specifically $\frac{1}{\Gamma} = 1$ fs and $\frac{1}{\Gamma} = 5$ fs. Due to the signal's exclusive sensitivity to electronic coherence in the molecule, the helical dichroism diffraction signal effectively tracks the time evolution of the electronic coherence, including its dephasing. This is a key advantage of using a coherence-only signal, as standard time-resolved diffraction signal will still exhibit strong time-dependent features from electronic populations, even after electronic coherence has completely decayed. Additionally, such coherence-only signal also has the unique benefit of detecting other critical coherent processes, such as electronic coherence generated at conical intersections. In such cases, the coherence-only signal can provide clear evidence of a conical intersection passage by isolating population contributions that are not specific to such events [17,53–55].

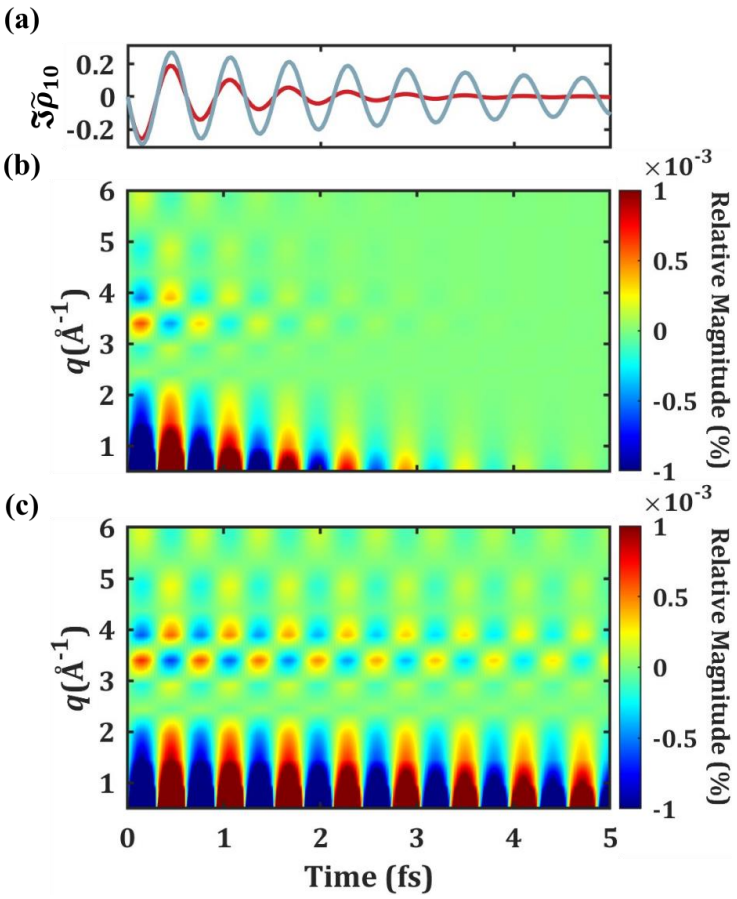

Figure 3. (a) The magnitude of the electronic coherence term ρ_{10} with two different dephasing rates: $\frac{1}{\Gamma} = 1$ fs (red) and $\frac{1}{\Gamma} = 5$ fs (azure). (b) The time-resolved helical dichroism diffraction signals ($l = \pm 1$) with a dephasing rate of $\frac{1}{\Gamma} = 1$ fs. (c) Same as (b), but with $\frac{1}{\Gamma} = 5$ fs.

A challenge in using vortex electron beams for UED is the phase singularity, which causes zero intensity at the beam center—an issue for both twisted X-rays and electrons. A tight focus of the vortex beam on the targeted sample is beneficial for achieving a noticeable effect. Previous studies indicate that a vortex beam focused to ~50 nm can have a substantial impact on molecules in a disordered sample [56,57]. Vortex electron beams have been generated at scales of a few hundred nanometers [29,58], and further technical advancements to reduce the size would enhance signal strength in the proposed method.

In summary, we have introduced a novel electron diffraction technique capable of directly monitoring transient electronic coherences in molecules. By analyzing the difference in the electron diffraction signal produced by vortex electron beams with opposite orbital angular momenta, we demonstrate that the time evolution of electronic coherences can be exclusively tracked. We applied this method to study early attosecond electron dynamics in oxazole following photoexcitation, capturing both its time evolution and the associated real-space electron density changes. We note that vortex electrons can also be applied for ordered samples, such as crystals, where two-molecule diffraction term dominates. This has been used to determine chirality of crystals and magnetic structures in materials [58–60]. Given that transient electronic coherences manifest also in two-molecule diffraction signals, the method described here could, in principle, be applied to ordered samples. However, addressing the dominant intermolecular structure form factor in Vortex-UED would be an interesting focus for future studies.

The proposed Vortex-UED is challenging and requires substantial technical development for experimental realization. Our study shows that the effort is worthwhile, as it provides a promising direction for the direct imaging of transient electronic coherences in molecules, and potentially in materials. The proposed technique holds potential for exploring other fundamental coherence phenomena, such as conical intersection passages and quantum transport. Furthermore, its ability to monitor electronic decoherence could be beneficial to research fields such as attosecond science and quantum computing.

Acknowledgements

This research was supported in part by W. M. Keck Foundation through computing resources at the W. M. Keck Laboratory for Integrated Biology at UC San Diego.

Competing interests

Authors declare that they have no competing interests.

Reference

[1] G. Hunter, Conditional probability amplitudes in wave mechanics, Int J of Quantum Chemistry **9**, 237 (1975).

[2] L. S. Cederbaum, The exact molecular wavefunction as a product of an electronic and a nuclear wavefunction, J. Chem. Phys. **138**, 224110 (2013).

[3] D. Strickland and G. Mourou, Compression of amplified chirped optical pulses, Opt. Commun. **55**, 447 (1985)

[4] A. H. Zewail, Femtochemistry: Atomic-Scale Dynamics of the Chemical Bond, J. Phys. Chem. A **104**, 5660 (2000).

[5] M. Hentschel, R. Kienberger, Ch. Spielmann, G. A. Reider, N. Milosevic, T. Brabec, P. Corkum, U. Heinzmann, M. Drescher and F. Krausz, Attosecond metrology, Nature (London), **414**, 509 (2001).

[6] P. M. Paul, E. S. Toma, P. Breger, G. Mullot, F. Augé, Ph. Balcou, H. G. Muller, and P. Agostini, Observation of a Train of Attosecond Pulses from High Harmonic Generation, Science **292**, 1689 (2001).

[7] G. D. Scholes, G. R. Fleming, L. X. Chen, A. Aspuru-Guzik, A. Buchleitner, D. F. Coker, G. S. Engel, R. van Grondelle, A. Ishizaki, D. M. Jonas, J. S. Lundeen, J. K. McCusker, S. Mukamel, J. P. Ogilvie, A. Olaya-Castro, M. A. Ratner, F. C. Spano, K. B. Whaley and X. Zhu, Using coherence to enhance function in chemical and biophysical systems, Nature (London) **543**, 647 (2017).

[8] J. Cao, R. J. Cogdell, D. F. Coker, H.-G. Duan, J. Hauer, U. Kleinekathöfer, T. L. C. Jansen, T. Mančal, R. J. D. Miller, J. P. Ogilvie, V. I. Prokhorenko, T. Renger, H.-S. Tan, R. Tempelaar, M. Thorwart, E. Thyrhaug, S. Westenhoff, D. Zigmantas, Quantum biology revisited, Sci. Adv. **6**, eaaz4888 (2020).

[9] M. R. Wasielewski, M. D. E. Forbes, N. L. Frank, K. Kowalski, G. D. Scholes, J. Yuen-Zhou, M. A. Baldo, D. E. Freedman, R. H. Goldsmith, T. Goodson III, M. L. Kirk, J. K. McCusker, J. P. Ogilvie, D. A. Shultz, S. Stoll and K. B. Whaley, Exploiting chemistry and molecular systems for quantum information science, Nat. Rev. Chem. **4**, 490 (2020).

[10] E. Goulielmakis, Z.-H. Loh, A. Wirth, R. Santra, N. Rohringer, V. S. Yakovlev, S. Zherebtsov, T. Pfeifer, A. M. Azzeer, M. F. Kling, S. R. Leone and F. Krausz, Real-time observation of valence electron motion, Nature (London) **466**, 739 (2010).

[11] F. Calegari, D. Ayuso, A. Trabattoni, L. Belshaw, S. De Camillis, S. Anumula, F. Frassetto, L. Poletto, A. Palacios, P. Decleva, J. B. Greenwood, F. Martín and M. Nisoli, Ultrafast electron dynamics in phenylalanine initiated by attosecond pulses, Science **346**, 336 (2014).

[12] P. M. Kraus, B. Mignolet, D. Baykusheva, A. Rupenyan, L. Horný, E. F. Penka, G. Grassi, O. I. Tolstikhin, J. Schneider, F. Jensen, L. B. Madsen, A. D. Bandrauk, F. Remacle, H. J. Wörner, Measurement and laser control of attosecond charge migration in ionized iodoacetylene, Science **350**, 790 (2015).

[13] T. Barillot, O. Alexander, B. Cooper, T. Driver, D. Garratt, S. Li, A. Al Haddad, A. Sanchez-Gonzalez, M. Agåker, C. Arrell, M. J. Bearpark, N. Berrah, C. Bostedt, J. Bozek, C. Brahms, P. H. Bucksbaum, A. Clark, G. Doumy, R. Feifel, L. J. Frasinski, S. Jarosch, A. S. Johnson, L. Kjellsson, P. Kolorenč, Y. Kumagai, E. W. Larsen, P. Matia-Hernando, M. Robb, J.-E. Rubensson, M. Ruberti, C. Sathe, R. J. Squibb, A. Tan, J. W. G. Tisch, M. Vacher, D. J. Walke, T. J. A. Wolf, D. Wood, V. Zhaunerchyk, P. Walter, T. Osipov, A. Marinelli, T. J. Maxwell, R. Coffee, A. A. Lutman, V. Averbukh, K. Ueda, J. P. Cryan and J. P. Marangos, Correlation-Driven Transient Hole Dynamics Resolved in Space and Time in the Isopropanol Molecule, Phys. Rev. X **11**, 031048 (2021).

[14] S. Li, T. Driver, P. Rosenberger, E. G. Champenois, J. Duris, A. Al-Haddad, V. Averbukh, J. C. T. Barnard, N. Berrah, C. Bostedt, P. H. Bucksbaum, R. N. Coffee, L. F. DiMauro, L. Fang, D. Garratt, A. Gatton, Z. Guo, G. Hartmann, D. Haxton, W. Helml, Z. Huang, A. C. LaForge, A. Kamalov, J. Knurr, M.-F. Lin, A. A. Lutman, J. P. MacArthur, J. P. Marangos, M. Nantel, A. Natan, R. Obaid, J. T. O'Neal, N. H. Shivaram, A. Schori, P. Walter, A. L. Wang, T. J. A. Wolf, Z. Zhang, M. F. Kling, A. Marinelli and J. P. Cryan, Attosecond coherent electron motion in Auger-Meitner decay, Science **375**, 285 (2022).

[15] D. Schwickert, M. Ruberti, P. Kolorenč, S. Usenko, A. Przystawik, K. Baev, I. Baev, M. Braune, L. Bocklage, M. K. Czwalinna, S. Deinert, S. Düsterer, A. Hans, G. Hartmann, C. Haunhorst, M. Kuhlmann, S. Palutke, R. Röhlsberger, J. Rönsch-Schulenburg, P. Schmidt, S. Toleikis, J. Viefhaus, M. Martins, A. Knie, D. Kip, V. Averbukh, J. P. Marangos and T. Laarmann, Electronic quantum coherence in glycine molecules probed with ultrashort x-ray pulses in real time, Sci. Adv. **8**, eabn6848 (2022).

[16] M. Kowalewski, K. Bennett, K. E. Dorfman, and S. Mukamel, Catching Conical Intersections in the Act: Monitoring Transient Electronic Coherences by Attosecond Stimulated X-Ray Raman Signals, Phys. Rev. Lett. **115**, 193003 (2015).

[17] H. Yong, J. R. Rouxel, D. Keefer, and S. Mukamel, Direct Monitoring of Conical Intersection Passage via Electronic Coherences in Twisted X-Ray Diffraction, Phys. Rev. Lett. **129**, 103001 (2022).

[18] Fast and furious X-ray free-electron lasers, Nat. Photon. **18**, 639 (2024).

[19] M. H. Pirenne, The Diffraction of X-Rays and Electrons by Free Molecules (Cambridge University Press, Cambridge, England; New York: Macmillan, 1946).

[20] J. C. H. Spence, Outrunning damage: Electrons vs X-rays—timescales and mechanisms, Struct. Dyn. **4**, 044027 (2017).

[21] L. Ma, H. Yong, J. D. Geiser, A. Moreno Carrascosa, N. Goff, and P. M. Weber, Ultrafast x-ray and electron scattering of free molecules: A comparative evaluation, Struct. Dyn. **7**, 034102 (2020).

[22] S. M. Lloyd, M. Babiker, G. Thirunavukkarasu, and J. Yuan, Electron vortices: Beams with orbital angular momentum, Rev. Mod. Phys. **89**, 035004 (2017).

[23] K.Y. Bliokh, I.P. Ivanov, G. Guzzinati, L. Clark, R. Van Boxem, A. Béché, R. Juchtmans, M.A. Alonso, P. Schattschneider, F. Nori, and J. Verbeeck, Theory and applications of free-electron vortex states, Phys. Rep. **690**, 1 (2017).

[24] B. J. McMorran, A. Agrawal, P. A. Ercius, V. Grillo, A. A. Herzing, T. R. Harvey, M. Linck, and J. S. Pierce, Origins and demonstrations of electrons with orbital angular momentum, Phil. Trans. R. Soc. A. **375**, 20150434 (2017).

[25] H. Larocque, I. Kaminer, V. Grillo, G. Leuchs, M. J. Padgett, R. W. Boyd, M. Segev, and E. Karimi, 'Twisted' electrons, Contemp Phys **59**, 126 (2018).

[26] M. Uchida and A. Tonomura, Generation of electron beams carrying orbital angular momentum, Nature (London) **464**, 737 (2010).

[27] B. J. McMorran, A. Agrawal, I. M. Anderson, A. A. Herzing, H. J. Lezec, J. J. McClelland, and J. Unguris, Electron Vortex Beams with High Quanta of Orbital Angular Momentum, Science **331**, 192 (2011).

[28] J. Handali, P. Shakya, and B. Barwick, Creating electron vortex beams with light, Opt. Express **23**, 5236 (2015).

[29] G. M. Vanacore, G. Berruto, I. Madan, E. Pomarico, P. Biagioni, R. J. Lamb, D. McGrouther, O. Reinhardt, I. Kaminer, B. Barwick, H. Larocque, V. Grillo, E. Karimi, F. J. García de Abajo and F. Carbone, Ultrafast generation and control of an electron vortex beam via chiral plasmonic near fields, Nat. Mater. **18**, 573 (2019).

[30] A. A. Ischenko, P. M. Weber, and R. J. D. Miller, Capturing Chemistry in Action with Electrons: Realization of Atomically Resolved Reaction Dynamics, Chem. Rev. **117**, 11066 (2017).

[31] M. Centurion, T. J. A. Wolf, and J. Yang, Ultrafast Imaging of Molecules with Electron Diffraction, Annu. Rev. Phys. Chem. **73**, 21 (2022).

[32] H. Yong, A. Kirrander, and P. M. Weber, *Time-Resolved X-Ray Scattering of Excited State Structure and Dynamics*, in *Structural Dynamics with X-Ray and Electron Scattering*, edited by K. Amini, A. Rouzée, and M. J. J. Vrakking (Royal Society of Chemistry, 2023), pp. 344–373.

[33] Y. Lee, K. Y. Oang, D. Kim, and H. Ihee, A comparative review of time-resolved x-ray and electron scattering to probe structural dynamics, Struct. Dyn. **11**, 031301 (2024).

[34] Q. Wang, L. Yun, and J. Yang, Ultrafast Molecular Movies: Probing Chemical Dynamics with Femtosecond Electron and X-Ray Diffraction, CCS Chem. **6**, 1092 (2024).

[35] J. R. Rouxel, D. Keefer, and S. Mukamel, Signatures of electronic and nuclear coherences in ultrafast molecular x-ray and electron diffraction, Struct. Dyn. **8**, 014101 (2021).

[36] J. R. Rouxel, D. Keefer, F. Aleotti, A. Nenov, M. Garavelli, and S. Mukamel, Coupled Electronic and Nuclear Motions during Azobenzene Photoisomerization Monitored by Ultrafast Electron Diffraction, J. Chem. Theory Comput. **18**, 605 (2022).

[37] M. Simmermacher, N. E. Henriksen, K. B. Møller, A. Moreno Carrascosa, and A. Kirrander, Electronic Coherence in Ultrafast X-Ray Scattering from Molecular Wave Packets, Phys. Rev. Lett. **122**, 073003 (2019).

[38] M. Simmermacher, A. Moreno Carrascosa, N. E. Henriksen, K. B. Møller, and A. Kirrander, Theory of ultrafast x-ray scattering by molecules in the gas phase, J. Chem. Phys. **151**, 174302 (2019).

[39] J. Jiang, M. Zhang, A. Gu, R. J. D. Miller, and Z. Li, Quantum tomography of molecules using ultrafast electron diffraction, J. Chem. Phys. **160**, 104101 (2024).

[40] H. Yong, S. Sun, B. Gu, and S. Mukamel, Attosecond Charge Migration in Molecules Imaged by Combined X-ray and Electron Diffraction, J. Am. Chem. Soc. **144**, 20710 (2022).

[41] K. Bennett, M. Kowalewski, J. R. Rouxel, and S. Mukamel, Monitoring molecular nonadiabatic dynamics with femtosecond X-ray diffraction, Proc. Natl. Acad. Sci. U.S.A. **115**, 6538 (2018).
[42] See Supplemental Material at [URL] for notes on (1) vortex ultrafast electron diffraction signal, (2) helical dichroism diffraction signal of Vortex-UED, (3) computational details, and (4) detection of electronic coherences arising from different electronic transitions, which includes Fig. S1-S4 and Refs. [43–46].
[43] H. Werner, P. J. Knowles, G. Knizia, F. R. Manby, and M. Schütz, Molpro: a general-purpose quantum chemistry program package, WIREs Comput Mol Sci **2**, 242 (2012).
[44] H.-J. Werner et al., The Molpro quantum chemistry package, The Journal of Chemical Physics **152**, 144107 (2020).
[45] Q. Sun et al., P Y SCF: the Python-based simulations of chemistry framework, WIREs Comput Mol Sci **8**, e1340 (2018).
[46] Q. Sun et al., Recent developments in the P Y SCF program package, The Journal of Chemical Physics **153**, 024109 (2020).
[47] P. Lokwani, B. P. Nagori, N. Batra, A. Goyal, S. Gupta, and N. Singh, Benzoxazole: The molecule of diverse biological activities, J. Chem. Pharm. Res. **3**, 302 (2011).
[48] N. Zeinali, I. Oluwoye, M. Altarawneh, and B. Z. Dlugogorski, Kinetics of Photo-Oxidation of Oxazole and its Substituents by Singlet Oxygen, Sci. Rep. **10**, 3668 (2020).
[49] J. Cao, Z.-Z. Xie, and X. Yu, Excited-state dynamics of oxazole: A combined electronic structure calculations and dynamic simulations study, Chem. Phys. **474**, 25 (2016).
[50] T. Geng, J. Ehrmaier, O. Schalk, G. W. Richings, T. Hansson, G. Worth, and R. D. Thomas, Time-Resolved Photoelectron Spectroscopy Studies of Isoxazole and Oxazole, J. Phys. Chem. A **124**, 3984 (2020).
[51] H. Yong, N. Zotev, J. M. Ruddock, B. Stankus, M. Simmermacher, A. M. Carrascosa, W. Du, N. Goff, Y. Chang, D. Bellshaw, M. Liang, S. Carbajo, J. E. Koglin, J. S. Robinson, S. Boutet, M. P. Minitti, A. Kirrander and P. M. Weber, Observation of the molecular response to light upon photoexcitation, Nat. Commun. **11**, 2157 (2020).
[52] S. Sun, H. Yong, F. Chen, and S. Mukamel, Coherent ring-current migration of Mg-phthalocyanine probed by time-resolved X-ray circular dichroism, Chem. Sci. **13**, 10327 (2022).
[53] D. Keefer, T. Schnappinger, R. De Vivie-Riedle, and S. Mukamel, Visualizing conical intersection passages via vibronic coherence maps generated by stimulated ultrafast X-ray Raman signals, Proc. Natl. Acad. Sci. U.S.A. **117**, 24069 (2020).
[54] S. M. Cavaletto, Y. Nam, J. R. Rouxel, D. Keefer, H. Yong, and S. Mukamel, Attosecond Monitoring of Nonadiabatic Molecular Dynamics by Transient X-ray Transmission Spectroscopy, J. Chem. Theory Comput. **19**, 2327 (2023).
[55] D. Keefer, S. M. Cavaletto, J. R. Rouxel, M. Garavelli, H. Yong, and S. Mukamel, Ultrafast X-Ray Probes of Elementary Molecular Events, Annu. Rev. Phys. Chem. **74**, 73 (2023).
[56] J. R. Rouxel, B. Rösner, D. Karpov, C. Bacellar, G. F. Mancini, F. Zinna, D. Kinschel, O. Cannelli, M. Oppermann, C. Svetina, A. Diaz, J. Lacour, C. David, and M. Chergui, Hard X-ray helical dichroism of disordered molecular media, Nat. Photon. **16**, 570 (2022).
[57] L. Ye, J. R. Rouxel, S. Asban, B. Rösner, and S. Mukamel, Probing Molecular Chirality by Orbital-Angular-Momentum-Carrying X-ray Pulses, J. Chem. Theory Comput. **15**, 4180 (2019).
[58] V. Grillo, T. R. Harvey, F. Venturi, J. S. Pierce, R. Balboni, F. Bouchard, G. Ca. Gazzadi, S. Frabboni, A. H. Tavabi, Z.-A. Li, R. E. Dunin-Borkowski, R. W. Boyd, B. J. McMorran, and E.

Karimi, Observation of nanoscale magnetic fields using twisted electron beams, Nat. Commun. **8**, 689 (2017).

[59] R. Juchtmans, A. Béché, A. Abakumov, M. Batuk, and J. Verbeeck, Using electron vortex beams to determine chirality of crystals in transmission electron microscopy, Phys. Rev. B **91**, 094112 (2015).

[60] R. Juchtmans and J. Verbeeck, Orbital angular momentum in electron diffraction and its use to determine chiral crystal symmetries, Phys. Rev. B **92**, 134108 (2015).

Supplementary Material for

Diffractive imaging of transient electronic coherences in molecules with electron vortices

Haowei Wu, Haiwang Yong*
*Correspondence to: hyong@ucsd.edu (H. Y.)

Note 1. Vortex Ultrafast Electron Diffraction Signal

The off-resonant single-molecule electron diffraction signal in the minimal coupling picture is given by [1–3]

$$S(\mathbf{q},T) \propto \frac{1}{q^4}\int d\mathbf{r}d\mathbf{r}'dtF_e(\mathbf{r},t-T)F_e^*(\mathbf{r}',t-T)\left\langle\left(\hat{\sigma}^{\mathrm{T}}\right)^{\dagger}(\mathbf{r}',t)\hat{\sigma}^{\mathrm{T}}(\mathbf{r},t)\right\rangle e^{i\mathbf{q}\cdot(\mathbf{r}-\mathbf{r}')} \tag{S1}$$

where F_e is the electron beam profile, $\hat{\sigma}^{\mathrm{T}}(\mathbf{r},t)=\hat{\sigma}^{\mathrm{E}}(\mathbf{r},t)+\hat{\sigma}^{\mathrm{N}}(\mathbf{r},t)$ is the total charge-density operator given by the sum of the electronic charge-density operator, $\hat{\sigma}^{\mathrm{E}}(\mathbf{r},t)$, and the nuclear charge-density operator, q is the magnitude of momentum transfer $\mathbf{q}$. The functions characterizing a vortex electron beam have a general form which can be written as [4]

$$F_e(\mathbf{r},t)=F(t)u(r,z)e^{il\phi} \tag{S2}$$

where $F(t)$ is the temporal profile, $u(r,z)$ is the radial profile of the beam at height z, l denotes the orbital angular momentum (OAM), and ϕ is the azimuthal angle in cylindrical coordinates. The exact form of $u(r,z)$ depends on the type of vortex beam [4]. Over the molecular scale, $u(r,z)$ can be treated as a constant. Substitute Eq. S2 into Eq. S1 we obtain for the Vortex-UED signal

$$S(\mathbf{q},T)\propto\int dt|F(t-T)|^2\tilde{S}_l(\mathbf{q},t) \tag{S3}$$

where $\tilde{S}_l(\mathbf{q},t)$ is the time-dependent molecular response carrying angular momentum l. It is defined as

$$\tilde{S}_l(\mathbf{q},t)=\frac{1}{q^4}\int d\mathbf{r}d\mathbf{r}'e^{il\phi}e^{-il\phi'}\left\langle\left(\hat{\sigma}^{\mathrm{T}}\right)^{\dagger}(\mathbf{r}',t)\hat{\sigma}^{\mathrm{T}}(\mathbf{r},t)\right\rangle e^{i\mathbf{q}\cdot(\mathbf{r}-\mathbf{r}')} \tag{S4}$$

The above integral can be divided into four terms by rewriting it with $\hat{\sigma}^{\mathrm{E}}(\mathbf{r},t)$ and $\hat{\sigma}^{\mathrm{N}}(\mathbf{r},t)$. Let $\hat{\sigma}^{\mathrm{K}}(\boldsymbol{r},t)$ denotes either $\hat{\sigma}^{\mathrm{E}}(\boldsymbol{r},t)$ or $\hat{\sigma}^{\mathrm{N}}(\boldsymbol{r},t)$. Eq. S4 can be written as

$$\tilde{S}_l(\mathbf{q},t)=\frac{1}{q^4}\left\langle\left(\hat{\sigma}_l^{\mathrm{T}}\right)^{\dagger}(\mathbf{q},t)\hat{\sigma}_l^{\mathrm{T}}(\mathbf{q},t)\right\rangle=\frac{1}{q^4}\left\langle\hat{\sigma}_{-l}^{\mathrm{T}}(-\mathbf{q},t)\hat{\sigma}_l^{\mathrm{T}}(\mathbf{q},t)\right\rangle \tag{S5}$$

where $\hat{\sigma}_l^{\mathrm{E/N}}(\mathbf{q},t)=\int d\mathbf{r}\hat{\sigma}^{\mathrm{E/N}}(\mathbf{r},t)e^{il\phi}e^{i\mathbf{q}\cdot\mathbf{r}}$. Since $\left(\hat{\sigma}^{\mathrm{E/N}}\right)^{\dagger}(\mathbf{r},t)=\hat{\sigma}^{\mathrm{E/N}}(\mathbf{r},t)$, we have

$$\left(\hat{\sigma}_l^{\mathrm{E/N}}\right)^{\dagger}(\mathbf{q},t)=\int d\mathbf{r}\hat{\sigma}^{\mathrm{E/N}}(\mathbf{r},t)e^{-il\phi}e^{-i\mathbf{q}\cdot\mathbf{r}}=\hat{\sigma}_{-l}^{\mathrm{E/N}}(-\mathbf{q},t). \tag{S6}$$

Substituting the time-dependent molecular many-electron wave function (Eq. 2 in main text) in Eq. S5, we obtain

$$\begin{aligned}q^4\tilde{S}_l(\mathbf{q},t)=&\sum_{k,m,j}\rho_{jk}(t)\sigma_{-l,km}^{\mathrm{E}}(-\mathbf{q})\sigma_{l,mj}^{\mathrm{E}}(\mathbf{q})+\sum_k\rho_{kk}(t)\sigma_{-l}^{\mathrm{N}}(-\mathbf{q})\sigma_l^{\mathrm{N}}(\mathbf{q})\\&+2\sum_{k,j}\Re\left[\rho_{jk}(t)\sigma_{-l,kj}^{\mathrm{E}}(-\mathbf{q})\sigma_l^{\mathrm{N}}(\mathbf{q})\right]\\=&\tilde{S}_{\mathrm{E},l}(\mathbf{q},t)+\tilde{S}_{\mathrm{N},l}(\mathbf{q},t)+\tilde{S}_{\mathrm{mix},l}(\mathbf{q},t)\end{aligned} \tag{S7}$$

$\tilde{S}_l(\mathbf{q},t)$ is divided into contributions from pure electronic term, pure nuclear term and a mixed contribution from both electrons and nuclei. Furthermore, the electronic contribution can be separated into two components: the population contribution and the coherence contribution.

$$\begin{aligned}\tilde{S}_{\mathrm{E},l}(\mathbf{q},t)=&\sum_{k,m}\rho_{kk}(t)\sigma_{-l,km}^{\mathrm{E}}(-\mathbf{q})\sigma_{l,mk}^{\mathrm{E}}(\mathbf{q})\\&+2\sum_{j>k}\Re\left[\rho_{jk}(t)\sum_m\sigma_{-l,km}^{\mathrm{E}}(-\mathbf{q})\sigma_{l,mj}^{\mathrm{E}}(\mathbf{q})\right]\end{aligned}$$

$$= \tilde{S}_{\mathrm{E},l}^{\mathrm{pop}}(\mathbf{q},t) + \tilde{S}_{\mathrm{E},l}^{\mathrm{coh}}(\mathbf{q},t). \tag{S8}$$

To simplify the expression, we define

$$\alpha_{\mathrm{E},l,kk}(\mathbf{q}) = \sum_m \sigma_{-l,km}^{\mathrm{E}}(-\mathbf{q})\sigma_{l,mk}^{\mathrm{E}}(\mathbf{q}), \tag{S9}$$

$$\beta_{\mathrm{E},l,kj}(\mathbf{q}) = \sum_m \sigma_{-l,km}^{\mathrm{E}}(-\mathbf{q})\sigma_{l,mj}^{\mathrm{E}}(\mathbf{q}), \tag{S10}$$

With similar treatment, the pure nuclear contribution is

$$\tilde{S}_{\mathrm{N},l}(\mathbf{q},t) = \sum_k \rho_{kk}(t)\sigma_{-l}^{\mathrm{N}}(-\mathbf{q})\sigma_l^{\mathrm{N}}(\mathbf{q}) = \sum_k \rho_{kk}(t)\alpha_{\mathrm{N},l}(\mathbf{q}). \tag{S11}$$

The mixed contribution can also be divided into population and coherence part:

$$\tilde{S}_{\mathrm{mix},l}(\mathbf{q},t) = \tilde{S}_{\mathrm{mix},l}^{\mathrm{pop}}(\mathbf{q},t) + \tilde{S}_{\mathrm{mix},l}^{\mathrm{coh}}(\mathbf{q},t), \tag{S12}$$

where

$$\begin{aligned}\tilde{S}_{\mathrm{mix},l}^{\mathrm{pop}}(\mathbf{q},t) &= 2\sum_k \Re\left[\rho_{kk}(t)\sigma_{-l,kk}^{\mathrm{E}}(-\mathbf{q})\sigma_l^{\mathrm{N}}(\mathbf{q})\right] \\ &= 2\sum_k \Re\left[\rho_{kk}(t)\alpha_{\mathrm{mix},l,kk}(\mathbf{q})\right]\end{aligned} \tag{S13}$$

$$\begin{aligned}\tilde{S}_{\mathrm{mix},l}^{\mathrm{coh}}(\mathbf{q},t) &= 4\sum_{j>k} \Re\left[\rho_{jk}(t)\right]\Re\left[\sigma_{-l,kj}^{\mathrm{E}}(-\mathbf{q})\sigma_l^{\mathrm{N}}(\mathbf{q})\right] \\ &= 4\sum_{j>k} \Re\left[\rho_{jk}(t)\right]\Re\left[\beta_{\mathrm{mix},l,kj}(\mathbf{q})\right]\end{aligned} \tag{S14}$$

Note 2. Helical Dichroism Diffraction Signal of Vortex-UED

The helical dichroism diffraction signal is defined as

$$\begin{aligned}\tilde{S}_{\delta l}(q,t) &= \left\langle \tilde{S}_l(\mathbf{q},t)\right\rangle_\Omega - \left\langle \tilde{S}_{-l}(\mathbf{q},t)\right\rangle_\Omega \\ &= \frac{1}{q^4}\left[S_{\mathrm{E},\delta l}(q,t) + S_{\mathrm{N},\delta l}(q,t) + S_{\mathrm{mix},\delta l}(q,t)\right],\end{aligned} \tag{S15}$$

where $\langle\cdots\rangle_\Omega$ represents the rotationally-averaged diffraction signal. Similar to Eq. S7, $S_{\delta l}(q,t)$ can be divided into three terms. Because $\alpha_{\mathrm{E},-l,kk}(\mathbf{q})$ is real, from Eq. S6 we get

$$\alpha_{\mathrm{E},-l,kk}(\mathbf{q}) = \sum_m \sigma_{l,km}^{\mathrm{E}}(-\mathbf{q})\sigma_{-l,mk}^{\mathrm{E}}(\mathbf{q}) = \alpha_{\mathrm{E},l,kk}^*(-\mathbf{q}) = \alpha_{\mathrm{E},l,kk}(-\mathbf{q}) \tag{S16}$$

Such relation does not hold for $\beta_{\mathrm{E},-l,kj}(\mathbf{q})$, we have

$$\beta_{\mathrm{E},-l,kj}(\mathbf{q}) = \sum_m \sigma_{l,km}^{\mathrm{E}}(-\mathbf{q})\sigma_{-l,mj}^{\mathrm{E}}(\mathbf{q}) = \beta_{\mathrm{E},l,kj}^*(-\mathbf{q}) \tag{S17}$$

We thus get $\tilde{S}_{\mathrm{E},\delta l}^{\mathrm{pop}}(q,t) = \left\langle \tilde{S}_{\mathrm{E},l}^{\mathrm{pop}}(\mathbf{q},t)\right\rangle_\Omega - \left\langle \tilde{S}_{\mathrm{E},-l}^{\mathrm{pop}}(\mathbf{q},t)\right\rangle_\Omega = \left\langle \tilde{S}_{\mathrm{E},l}^{\mathrm{pop}}(\mathbf{q},t)\right\rangle_\Omega - \left\langle \tilde{S}_{\mathrm{E},l}^{\mathrm{pop}}(-\mathbf{q},t)\right\rangle_\Omega = 0$.

$\tilde{S}_{\mathrm{E},\delta l}(q,t)$ is then given by

$$\begin{aligned}\tilde{S}_{\mathrm{E},\delta l}(q,t) &= \left\langle \tilde{S}_{\mathrm{E},l}^{\mathrm{coh}}(\mathbf{q},t)\right\rangle_\Omega - \left\langle \tilde{S}_{\mathrm{E},-l}^{\mathrm{coh}}(\mathbf{q},t)\right\rangle_\Omega \\ &= 2\sum_{j>k}\left\{\Re\left[\rho_{jk}(t)\left\langle\beta_{\mathrm{E},l,kj}(\mathbf{q})\right\rangle_\Omega\right] - \Re\left[\rho_{jk}(t)\left\langle\beta_{\mathrm{E},l,kj}^*(-\mathbf{q})\right\rangle_\Omega\right]\right\} \\ &= 2\sum_{j>k}\Re\left[\rho_{jk}(t)\beta_{\mathrm{E},l,kj}(q)\right] - 2\sum_{j>k}\Re\left[\rho_{jk}(t)\beta_{\mathrm{E},l,kj}^*(q)\right] \\ &= -4\sum_{j>k}\Im\rho_{jk}(t)\Im\beta_{\mathrm{E},l,kj}(q)\end{aligned} \tag{S18}$$

Similarly, it is straightforward to get $\tilde{S}_{\mathrm{N},\delta l}(q,t)=0$ since $\alpha_{\mathrm{N},-l,kk}(\mathbf{q})=\alpha_{\mathrm{N},l,kk}(-\mathbf{q})$.
For the mixed contribution, signals with opposite OAM are related by

$$\alpha_{\mathrm{mix},-l,kk}(\mathbf{q})=\sigma^{\mathrm{E}}_{l,kk}(-\mathbf{q})\sigma^{\mathrm{N}}_{-l}(\mathbf{q})=\alpha^{*}_{\mathrm{mix},l,kk}(-\mathbf{q}), \tag{S19}$$

$$\beta_{\mathrm{mix},-l,kj}(\mathbf{q})=\sigma^{\mathrm{E}}_{l,kj}(-\mathbf{q})\sigma^{\mathrm{N}}_{-l}(\mathbf{q})=\beta^{*}_{\mathrm{mix},l,kj}(-\mathbf{q}). \tag{S20}$$

We get

$$\begin{aligned}\tilde{S}^{\mathrm{pop}}_{\mathrm{mix},\delta l}(q,t)&=\left\langle\tilde{S}^{\mathrm{pop}}_{\mathrm{mix},l}(\mathbf{q},t)\right\rangle_{\Omega}-\left\langle\tilde{S}^{\mathrm{pop}}_{\mathrm{mix},-l}(\mathbf{q},t)\right\rangle_{\Omega}\\&=2\sum_{k}\Re\left[\rho_{kk}(t)\left\langle\alpha_{\mathrm{mix},l,kk}(\mathbf{q})\right\rangle_{\Omega}-\rho_{kk}(t)\left\langle\alpha_{\mathrm{mix},-l,kk}(\mathbf{q})\right\rangle_{\Omega}\right]\\&=2\sum_{k}\Re\left[\rho_{kk}(t)\left\langle\alpha_{\mathrm{mix},l,kk}(\mathbf{q})\right\rangle_{\Omega}-\rho_{kk}(t)\left\langle\alpha^{*}_{\mathrm{mix},l,kk}(-\mathbf{q})\right\rangle_{\Omega}\right]\\&=2\sum_{k}\Re\left[\rho_{kk}(t)\alpha_{\mathrm{mix},l,kk}(q)-\rho_{kk}(t)\alpha^{*}_{\mathrm{mix},l,kk}(q)\right]\\&=0\end{aligned} \tag{S21}$$

and

$$\begin{aligned}\tilde{S}^{\mathrm{coh}}_{\mathrm{mix},\delta l}(q,t)&=\left\langle\tilde{S}^{\mathrm{coh}}_{\mathrm{mix},l}(\mathbf{q},t)\right\rangle_{\Omega}-\left\langle\tilde{S}^{\mathrm{coh}}_{\mathrm{mix},-l}(\mathbf{q},t)\right\rangle_{\Omega}\\&=4\sum_{j>k}\Re\left[\rho_{jk}(t)\right]\left\{\Re\left[\left\langle\beta_{\mathrm{mix},l,kj}(\mathbf{q})\right\rangle_{\Omega}\right]-\Re\left[\left\langle\beta^{*}_{\mathrm{mix},l,kj}(-\mathbf{q})\right\rangle_{\Omega}\right]\right\}\\&=4\sum_{j>k}\Re\left[\rho_{jk}(t)\right]\left\{\Re\left[\beta_{\mathrm{mix},l,kj}(q)\right]-\Re\left[\beta^{*}_{\mathrm{mix},l,kj}(q)\right]\right\}\\&=0\end{aligned} \tag{S22}$$

In summary, we get the final expression for the helical dichroism diffraction signal

$$\tilde{S}_{\delta l}(q,t)=S_{\mathrm{E},\delta l}(q,t)=-\frac{4}{q^{4}}\sum_{j>k}\Im\rho_{jk}(t)\Im\beta_{\mathrm{E},l,kj}(q) \tag{S23}$$

The electronic decoherence effect can be accounted for by multiplying $\rho_{jk}(t)$ with an exponential factor, given by $\rho_{jk}(t)e^{-\Gamma \mathrm{t}}=\tilde{\rho}_{jk}(t)$. [5] The Eq. S23 then becomes

$$\tilde{S}_{\delta l}(q,t)=-\frac{4}{q^{4}}\sum_{j>k}\Im\tilde{\rho}_{jk}(t)\Im\beta_{\mathrm{E},l,kj}(q) \tag{S24}$$

Note 3. Computational Details

The geometry of neutral ground state of oxazole was optimized using the SS-CAS(6,10)/aug-cc-pVDZ method. To compute the six lowest singlet valence excited states, including two valence states and four Rydberg states, the SA7-CAS(6,10)/aug-cc-pVDZ approach was employed. The active space, consisting of six electrons in ten orbitals, was chosen based on previous studies demonstrating its necessity for accurately describing the excited states of oxazole [6]. The complete active space self-consistent field (CASSCF) calculations were carried out using the Molpro electronic structure software package [7,8]. The electronic charge densities and transition charge densities in **q**-space were evaluated from the state specific charge density matrices, P^{jk}_{rs}, according to

$$\sigma^{\mathrm{E}}_{jk}(\mathbf{q})=\int d\mathbf{r}e^{i\mathbf{q}\cdot\mathbf{r}}\sigma^{\mathrm{E}}_{jk}(\mathbf{r})=\int d\mathbf{r}e^{i\mathbf{q}\cdot\mathbf{r}}\textstyle\sum_{rs}P^{jk}_{rs}\chi_{r}(\mathbf{r})\chi^{*}_{s}(\mathbf{r}) \tag{S25}$$

where $\chi_{r}(\mathbf{r})$ is an atomic basis function for the r_{th} atomic orbital, j and k are labels for adiabatic electronic states. The grid-based $\sigma^{\mathrm{E}}_{jk}(\mathbf{r})$ in real space was calculated from charge density matrices using PySCF software [9,10]. The nuclear charge density in **q**-space for a given nuclear structure was calculated as

$$\sigma^{\mathrm{N}}(\mathbf{q})=\textstyle\sum_{a}Z_{a}e^{i\mathbf{q}\cdot\mathbf{R}_{a}} \tag{S26}$$

where a labels the a_{th} atom with atomic number Z_{a} at position $\mathbf{R}_{a}$. The vortex-UED signals and their rotational averaging were calculated numerically. In Figure 3 we assumed an impulsive electron probe pulse.

In practice, the temporal pulse width needs to be shorter than the oscillation period of the system's electronic coherence to resolve the desired coherence signal.

Note 4. Detection of Electronic Coherences Arising From Different Electronic Transitions

In addition to the simulated signals for the electronic coherence arising from excitation to the $\pi\pi^*$ state discussed in the main text, we also present the simulated signals for the electronic coherence arising from excitation to the 3s Rydberg state in Figure S4. Since the phase twist, $e^{il\phi}$, with different topological charges modifies the electronic charge density in space differently, as given by Eq. S6, the resulting helical dichroism signal exhibits varying sensitivity to the electronic coherence density. This leads to more or fewer features along q, as illustrated in Figure S3 and Figure S4 for different electronic transitions. For example, $l = \pm 2$ displays more features for excitation to the $\pi\pi^*$ state compared $l = \pm 1$ and $l = \pm 3$, while $l = \pm 1$ exhibits distinct features (particularly the node around 0.9 $Å^{-1}$) for the excitation to 3s state compared to the other two. This suggests that carefully choosing the topological charges can enhance the sensitivity to a particular electronic transition of interest.

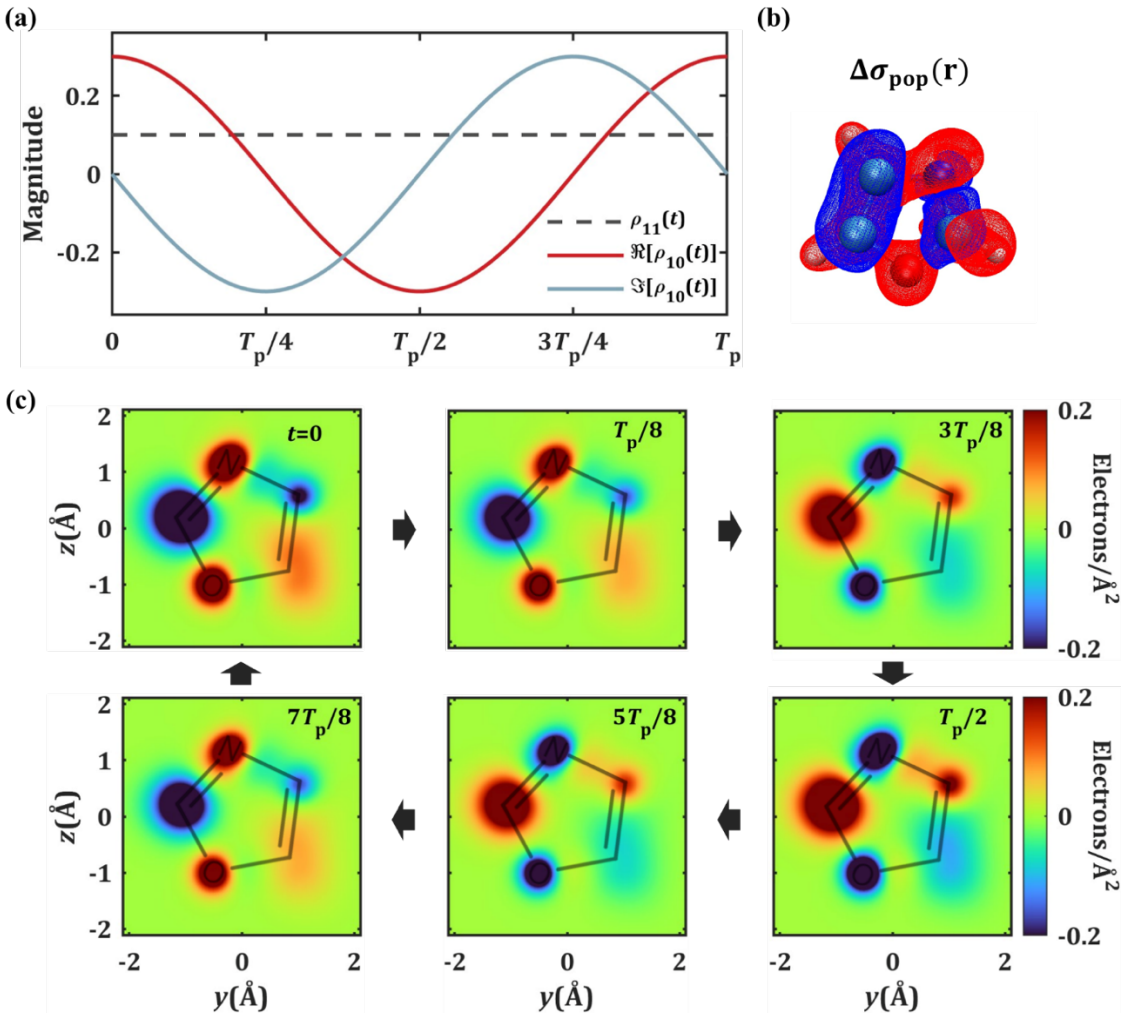

Figure S1. (a) The magnitude of the electronic population term ρ_{11} and the electronic coherence term ρ_{10} over a complete period. (b) Isosurface of the difference in electronic population density in real space, $\Delta\sigma^{\mathrm{E}}_{\mathrm{pop}}(\mathbf{r}) = \sigma^{\mathrm{E}}_{\mathrm{pop}}(\mathbf{r}) - \sigma^{\mathrm{E}}_{0}(\mathbf{r})$, where $\sigma^{\mathrm{E}}_{0}(\mathbf{r})$ represents the electronic charge density of the ground-state oxazole before excitation. (c) Evolution of the difference in electronic coherence density in real space, $\Delta\sigma^{\mathrm{E}}_{\mathrm{coh}}(\mathbf{r}, t) = \sigma_{\mathrm{coh}}(\mathbf{r}, t)$, where the electronic coherence density of the ground-state molecules is zero. Six different time points within one period are chosen for illustration. The charge densities are shown in the y-z plane by integrating over the x. An animation of the full attosecond electron dynamics following excitation to the $\pi\pi^*$ state with more time points is shown in the Supplementary Material.

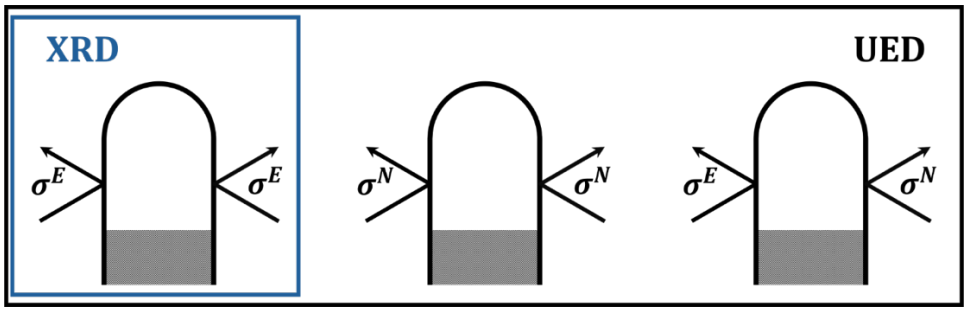

Figure S2. Loop diagrams for time-resolved single-molecule x-ray (blue box) and electron diffraction (black box).

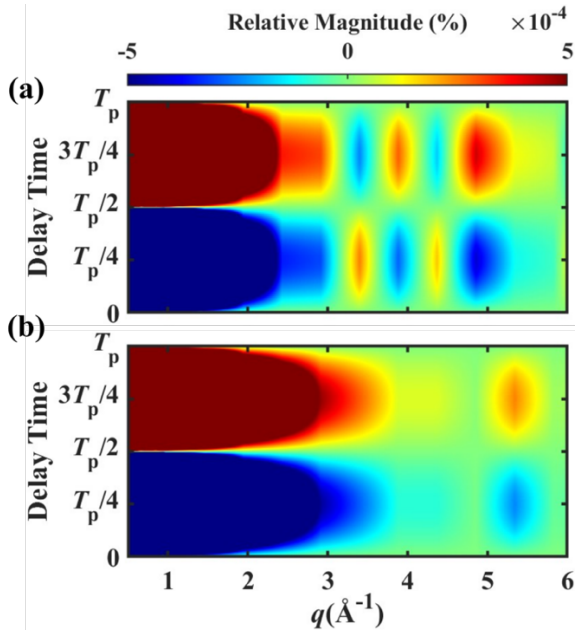

Figure S3. The helical dichroism diffraction signals in Equation S23 of attosecond electron dynamics following excitation to the ππ* state over a complete period for (a) $l = \pm 2$ and (b) $l = \pm 3$. The signals are shown as percentages, $\%S_{\delta l}(q,T) = 100\frac{S_{\delta l}(q,T)}{S_l^{\text{off}}(q)}$, where $S_l^{\text{off}}(q)$ is the reference Vortex-UED signal before time zero.

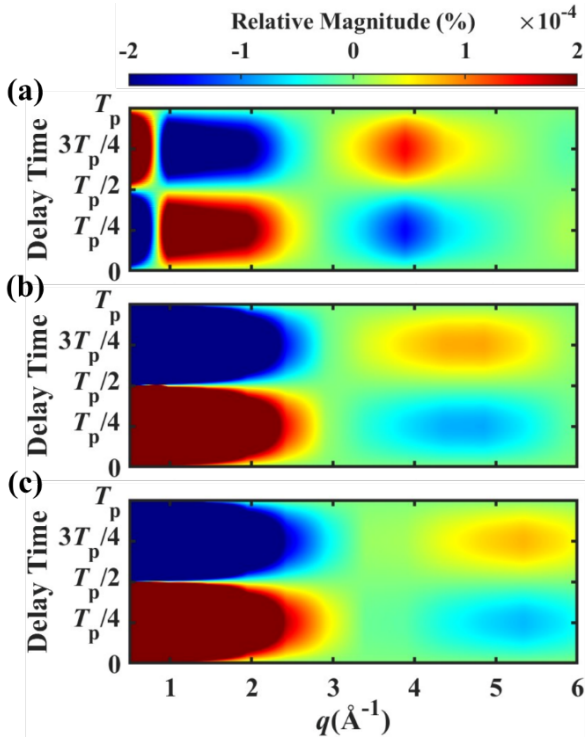

Figure S4. Same with Figure S3 but for the dynamics of oxazole following excitation to the 3s (πσ*) Rydberg state for (a) $l = \pm 1$, (b) $l = \pm 2$, and (c) $l = \pm 3$.

Supplementary References

[1] K. Bennett, M. Kowalewski, J. R. Rouxel, and S. Mukamel, Monitoring molecular nonadiabatic dynamics with femtosecond X-ray diffraction, Proc. Natl. Acad. Sci. U.S.A. **115**, 6538 (2018).

[2] J. R. Rouxel, D. Keefer, and S. Mukamel, Signatures of electronic and nuclear coherences in ultrafast molecular x-ray and electron diffraction, Structural Dynamics **8**, 014101 (2021).

[3] H. Yong, S. Sun, B. Gu, and S. Mukamel, Attosecond Charge Migration in Molecules Imaged by Combined X-ray and Electron Diffraction, J. Am. Chem. Soc. **144**, 20710 (2022).

[4] S. M. Lloyd, M. Babiker, G. Thirunavukkarasu, and J. Yuan, Electron vortices: Beams with orbital angular momentum, Rev. Mod. Phys. **89**, 035004 (2017).

[5] S. Sun, H. Yong, F. Chen, and S. Mukamel, Coherent ring-current migration of Mg-phthalocyanine probed by time-resolved X-ray circular dichroism, Chem. Sci. **13**, 10327 (2022).

[6] T. Geng, J. Ehrmaier, O. Schalk, G. W. Richings, T. Hansson, G. Worth, and R. D. Thomas, Time-Resolved Photoelectron Spectroscopy Studies of Isoxazole and Oxazole, J. Phys. Chem. A **124**, 3984 (2020).

[7] H. Werner, P. J. Knowles, G. Knizia, F. R. Manby, and M. Schütz, Molpro: a general-purpose quantum chemistry program package, WIREs Comput Mol Sci **2**, 242 (2012).

[8] H.-J. Werner et al., The Molpro quantum chemistry package, The Journal of Chemical Physics **152**, 144107 (2020).

[9] Q. Sun et al., P Y SCF: the Python-based simulations of chemistry framework, WIREs Comput Mol Sci **8**, e1340 (2018).

[10] Q. Sun et al., Recent developments in the P Y SCF program package, The Journal of Chemical Physics **153**, 024109 (2020).